Cancer Nanotechnology

RESEARCH Open Access

Perovskite quantum dots modulating upconversion nanomaterials for cancer early detections

Yue He[1], Hongtao Rao[1], JingJing Wang[1], Ying Wu[1], Caiqin Han[1], Changchun Yan[1], Hunter Temple[2], Le Zhang[1], Wei Chen[2,3*] and Ying Liu[1,4*]

*Correspondence: weichen@uta.edu; liuying@jsnu.edu.cn

[1] Jiangsu Key Laboratory of Advanced Laser Materials and Devices, School of Physics and Electronic Engineering, Jiangsu Normal University, Xuzhou, China
[2] Department of Physics, The University of Texas at Arlington, Arlington, TX, USA
[3] Medical Technology Research Centre, Anglia Ruskin University, Chelmsford Campus, Chelmsford CM1 1SQ, UK
[4] Xuzhou college of industrial technology, Xuzhou, China

Abstract

The accurate diagnosis and treatment of cancer cell lesions need a high standard of detection technology. Fluorescent probes to perform cancer biomarker detection have become a popular research issue. However, fluorescent probes still face enormous challenges of complex design and difficult detection. In this work, we propose a novel composite material UCNP@SiO_2 + QDs based on the combination of rare earth upconversion (UCNPs) and perovskite quantum dots (QDs) and design a new fluorescent probe MB-UCNP@SiO_2 + QDs with molecular beacon (MB) as the carrier, that can be excited by near-infrared light, emitted in the visible wavelength, specifically identified and highly sensitive. Under the excitation of 980 nm near-infrared light, the UCNPs and QDs in the composite produced the maximum efficiency of energy transfer through fluorescence resonance, and the multi-emission light of UCNPs synergistically excited the re-emission of QDs, and the energy transfer efficiency is 70.6%. By changing the doping ratio of QDs halogen elements in UCNP@SiO_2 + QDs, it is possible to modulate the precise luminescence of UCNP@SiO_2 + QDs in the entire wavelength range of visible light at different positions. The novel fluorescent probe is obtained using UCNP@SiO_2 + QDs and Black Hole Quencher-1 (BHQ1) quenching groups linked to the two respective sides of MB, selecting as the target of detection the myeloma cancer biomarker miRNA-155, a difficult diagnostic and complex developmental type, and have achieved specific recognition and low concentration of miRNA-155 and a detection limit of 73.5 pM. This fluorescent probe design can provide new ideas for the early diagnosis and treatment of cancer, tumors, and cardiovascular diseases.

Keywords: Upconversion, Perovskite quantum dots, Fluorescence resonance, MiRNA-155

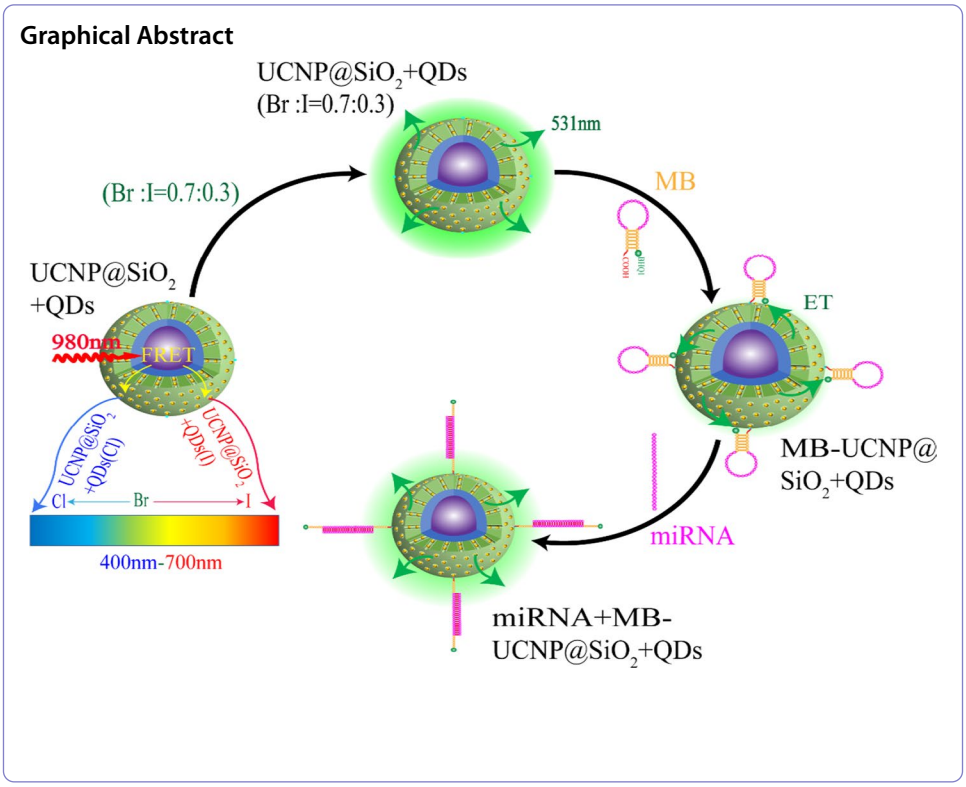

Introduction

MicroRNAs (miRNAs) are a type of single-stranded RNA, which generally has 21–25 bases (Ma et al. 2018). Most cellular lesions leading to cancer cell mutations are associated with abnormal overexpression of specific miRNAs, and effective detection of miRNAs plays an extremely important role in the diagnosis, treatment, and prevention of cancer (Lv et al. 2019; Zhang et al. 2019). There has been an endeavor to propose strategies for efficient and accurate multiplexed detection of miRNAs, and a variety of detection techniques for miRNAs have proven to be effective and practical. However, because miRNAs are expressed at extremely low concentrations and vary at different stages of development, there is a need to develop more sensitive and effective miRNAs detection methods. Current miRNA detection methods include electrochemistry (Labib et al. 2013), microarrays (Lim et al. 2005), electrochemiluminescence (ECL) (Liu et al. 2017a, b), fluorescence analysis (Zhang et al. 2020), colorimetric assays (Li et al. 2017), and surface enhanced Raman scattering (SERS) (Zhou et al. 2017). Fluorescent probe detection is recognized as a highly cost-effective method for miRNA determination because of its good selectivity, sensitivity, rapid response, operation feasibility, and biocompatibility (Hwang et al. 2010). Traditional fluorescent probe materials, such as organic dyes (Liu et al. 2017a, b; Pandey et al. 2022), fluorescent proteins (Kowada et al. 2015; Lu et al. 2019), quantum dots (Stanisavljevic et al. 2015; Martynenko et al. 2017; Chen 2008; Gao et al. 2021), carbon dots and graphene dots (Ke et al. 2013; Tang et al. 2021; Xu et al. 2021), etc., seriously interfere with multi-biomolecular fluorescence detection because the excitation light sources are generally UV or visible light, with broad and asymmetric fluorescence

emission peaks, severe tailing, and overlapping of various dye spectra with each other, together with very strong biological self-fluorescence (background fluorescence) and scattered light (Meng et al. 2020; Cu et al. 2019; Mao et al. 2017). In comparison, UCNPs are used with near-infrared light as the excitation light and the emission band are in the visible band; there is no scattered light or other fluorescence interference. In addition, the autofluorescence background of biological tissues is lower, the penetration depth is stronger with multi-wavelength luminescence, almost non-toxic, fluorescence intensity and high stability, and is currently a commonly used fluorescent probe material. In recent years, UCNPs materials have been rapidly developed in bioassays due to their special luminescent properties. The most common efficient UCNPs systems use Yb^{3+} as the sensitization ion, Er^{3+}, Tm^{3+}, Ho^{3+}, $Nd^{3+,}$ Pr^{3+}, and other luminescent ions (Chien et al. 2020; Yun et al. 2021), and fluoride (e.g., β-$NaYF_4$) as the doping substrate. In particular, $NaYF_4$ is currently recognized internationally as the most effective blue–green light UCNPs luminescent substrate material (Shan et al. 2010; Li et al. 2007). Ding et al. prepared carboxylated protein-modified UCNPs fluorescent probes, which are capable of achieving the detection of various specific miRNAs (Ding et al. 2022). However, the discrete energy levels and fixed emission bands of rare-earth ions make it difficult to match the optimal absorption properties of the measured targets, and cannot achieve a precise identification of the measured targets.

QDs have attracted increasing attention from more and more researchers due to their advantages, such as tunable emission wavelength, luminescent color diversity, high fluorescence quantum efficiency, narrow emission bands, and less susceptibility to spectral overlap (Li et al. 2016; Zhang et al. 2017; (Wang et al. 2021a, b). Wang et al. achieved a quantum dot-molecular beacon functionalized QD-MB@MoS_2 fluorescence in two emission bands with the control of the quantum dots size of a shell-core structure probe, and achieved the binary detection of multiple myeloma (MM)-associated miRNA-155 and miRNA-150 (Wang et al. 2022a, b). The position of the emission peak of quantum dots can generally be modulated by doping elements and size, and the method is simple and easy to implement as well as widely used. Compared with the conventional cadmium-based and indium-based quantum dots, QDs can simply be modified to cover a wide spectral range of visible light by modulating their halogen element (X = Cl, Br, I) ratio, and they can also be fine-tuned by adjusting the size to optimize the peak position. Li et al. used sulfobutylether-β-cyclodextrin to encapsulate $CsPbBr_3$ to form nanocomposites ($CsPbBr_3$@SBE-β-CD) as a fluorescent probe and successfully detected low concentrations of hydrogen sulfide material in the organs of adult zebrafish (Li et al. 2022). However, the process of QDs with different halogen elements to achieve spectral tuning could lead to instability in its own structure, which was highly sensitive to materials such as oxygen and water, which seriously hindered its development process. Generally, it need surface passivation and modification strategies to alleviate this problem, and a number of researchers have used silica-covered quantum dots and embedded chalcogenide nanocrystals in mesoporous silica to improve the stability (Wang et al. 2016a, b; Dirin et al. 2016).

If we combine UCNPs material and the QDs, it is possible that through QDs to compensate for the shortage of rare earth ions that are unable to be tolerated at visible

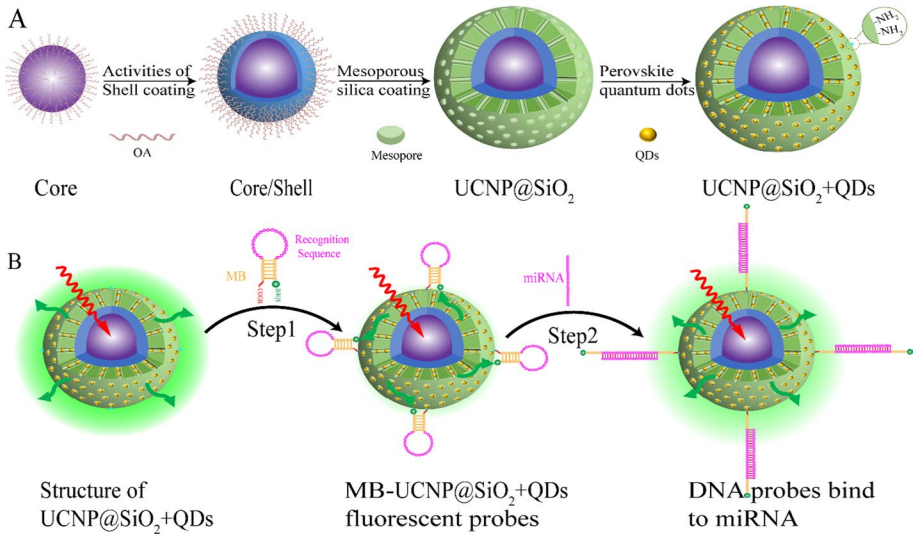

Fig. 1 Schematic diagram of the preparation and principle of the novel fluorescent probe MB-UCNP@SiO_2 + QDs based on the combination of UCNPs and QDs. **A** Preparation process of the novel composite material UCNP@SiO_2 + QDs. **B** Detection process of miRNA by the novel fluorescent probe MB-UCNP@SiO_2 + QDs

wavelengths for their separated energy levels, which can overcome the limitations of their respective applications in biofluorescence detection. With UCNPs as the donor and QDs as the acceptor, fluorescence resonance energy transfer (FRET) between them, under the excitation of near-infrared excitation light, and by changing the doping ratio and size of QDs in the composites, the composites can be precisely tuned in the visible band to achieve tunable multicolor luminescence (Ma et al. 2022; Zheng et al. 2018). Researchers used lanthanide-doped nanoparticle sensitization to fine-tune inorganic UCNPs luminescence among QDs to achieve panchromatic luminescence in the visible range (Xie et al. 2021). However, all the current research performed on the combination of UCNPs and QDs is limited to multicolor imaging systems, multicolor anti-counterfeiting, and tuned luminescence sensors, and is relatively scarce in biological detection (Fan et al. 2019).

In this work, we designed a new composite fluorescent probe MB-UCNP@SiO_2 + QDs based on the combination of UCNPs nanomaterials and QDs, which achieved both low concentration detection and specific recognition of the multiple myeloma biomarker miRNA-155. With UCNPs as the core structure, the shell uses mesoporous SiO_2 to cover UCNPs, and QDs are grown in situ in the mesopores of SiO_2 to obtain the new composite material UCNP@SiO_2 + QDs, and both of them make the multi-emission light of UCNPs re-excite QDs through FRET, and by modulating the doping ratio of halogen elements of QDs in UCNP@SiO_2 + QDs, which can accurately modulate the luminescence in the visible wavelength range (Fig. 1A). If the doping ratio of QDs halogen elements in UCNP@SiO_2 + QDs was Br: I = 0.7: 0.3, the emission peak of UCNP@SiO_2 + QDs modulated at 531 nm overlaps with the position of the strong absorption peak of the BHQ1 quenching group, and the best

fluorescence quenching effect could be accomplished. The UCNP@SiO_2 + QDs and BHQ1 quenching groups were connected at the two sides of MB to obtain the MB-UCNP@SiO_2 + QDs novel fluorescent probe (Fig. 1B, step 1). When the fluorescent probe was attached to the target miRNA-155, the structural loop of the molecular beacon MB was opened and the BHQ1 quenching group was moved away from the composite luminescent material, so that the fluorescence of UCNP@SiO_2 + QDs at 531 nm could be restored. In this way, we could accomplish the detection of the multiple myeloma biomarker miRNA-155 (Fig. 1B, step 2).

Materials and methods

Materials

Yttrium chloride hexahydrate ($YCl_3 \cdot 6H_2O$, 99.9%), Ytterbium chloride hexahydrate ($YbCl_3 \cdot 6H_2O$, 99.9%), Thulium chloride hexahydrate ($TmCl_3 \cdot 6H_2O$,99.9%), Oleic acid (OA, 99.7%), 1-octadecene (ODE, 95%), Ammonium fluoride (NH_4F,96%), Cyclohexane (C_6H_{12}, 99.5%), Methanol (CH_3OH, 99.5%), cesium carbonate (CS_2CO_3, 99%), lead chloride ($PbCl_2$, 99.9%), lead bromide ($PbBr_2$, 99%) lead iodide (PbI_2, 98%), oleylamine (OAM, 99.7%), cetyltrimethylammonium bromide (CTAB, 99%), ethyl orthosilicate (TEOS, 99.7%), 3-aminopropyltriethoxysilane (APTES, 99%) were purchased from Sangon Biotech Co.Ltd (Shanghai, China). Hydrochloric acid (HCl, 96%), ammonia ($NH_3 \cdot H_2O$, wt = 28%), hexane (C_6H_{14}, 99.7%), 1-ethyl-(3-dimethylaminopropyl) diimine carbonate hydrochloride (EDC, 98%) were purchased from Sinopharm Chemical Reagent Co.Ltd(Shanghai, China). N-Hydroxysuccinimide (NHS, 98%) was purchased from Macklin Biochemical Co.Ltd(Shanghai, China), anhydrous ethanol (C_2H_6O, 99.7%), sodium hydroxide (NaOH, 96%) were purchased from Xilong Chemical Co.Ltd(Shanghai, China), with the molecular beacon MB-155, miRNA-141, miRNA-21 and random rRNA corresponding base sequences were shown in Table 1. Ultrapure water was obtained from Water Purification Systems (H20BASIC-B, Sartorius, Germany).

Materials characterization

The experiments were performed with an intelligent digital display magnetic stirrer (ZNCL-TS-250 ml, Shanghai Anchun Instruments Co.Ltd, China) for the preparation of UCNPs and quantum dot nanomaterials, and an X-ray powder diffractometer (X-ray Diffraction, XRD, D8 ADVANCE, Bruker, Germany) for the physical phase analysis of UCNPs and QDs nanomaterials, respectively. The XRD was used to analyze UCNPs and QDs nanomaterials separately. Transmission Electron Microscopy (TEM, FEI TECNAI G2 F20) was used to characterize the morphology of UCNPs and QDs nanomaterials, respectively. A specific surface area analyzer (Brunauer–Emmet–Teller, Conta Instruments, USA) was used to analyze the adsorption and pore number of mesoporous silica. A fluorescence spectrophotometer (F-4600, Hitachi, Japan) was used to measure the QDs fluorescence spectra. 980 nm fiber laser (BOT980-5 W, Xi'an Laser Electronics

Technology Co.Ltd, China) was used to measure the UCNPs and UCNP@SiO_2 + QDs fluorescence spectra. UCNPs and QDs nanomaterial absorption spectra were measured separately using a UV–Vis–NIR spectrophotometer (Lambda 950, Perkin Eimer, USA). The infrared absorption spectra were measured by an FTIR spectrometer (Tensor 27, Bruker, Germany). All pipette tips, tubes and reagents were autoclaved by an autoclave (GI-54DWS, Shanghai Danding International Trading Co.Ltd, China).

Synthesis of UCNP@SiO_2 + QDs

The in-situ growth method was used to grow QDs in mesoporous SiO_2 (Chen et al. 2019; Huang et al. 2020; Malgras et al. 2016). Firstly, CS_2CO_3 and PbX_2 powder were respectively used to prepare CS precursor solution and PbX_2(Cl, Br, I) precursor solution. Under N_2 protection, a mixture of 20 mg of mesoporous UCNP@SiO_2 was dispersed in 0.5 ml of OA, 0.5 ml of OAM and 5 ml of ODE, heating up to 80 ℃ and agitating for 30 min, so that UCNP@SiO_2 was completely dispersed in the solution. And 2 ml of PbX_2 solution was injected rapidly, stirring was continued for 30 min, so that after heating up to 140 ℃, 2 ml of Cs prerequisites were injected into the solution to make Cs ions interact with PbX_2 ions in SiO_2 mesopores in situ, and when the solution was clearly clarified, it was quickly cooled down to room temperature by using an ice water bath. Finally, centrifugation with hexane was used to remove the excess QDs and dried overnight in a vacuum chamber to obtain the new UCNP@SiO_2 + QDs composites. Finally, the principle of APTES microhydrolysis was used to achieve amination on the surface of the composite particles (Li et al. 2020; Wang et al. 2020), which was used as a backup for the preparation of fluorescent probes later.

Synthesis of MB-UCNP@SiO_2 + QDs

A total of 20 mg of the aminated nanomaterial UCNP@SiO_2 + QDs was dispersed in 1 ml of ethanol solution, 5 mg of EDC and 5 mg of NHS were added to the solution and shaken to make it fully dissolved. The pH was adjusted with 2 μM hydrochloric acid solution to make the pH around 6.5, and the reaction was shaken for 30 min at room temperature to activate the amino group. Take out the carboxylated modified MB tube and prepare the MB solution with a concentration of 1 μM. The reaction was carried out by centrifugation at 10,000 rpm/min for 5 min and then stored at an environmental condition of 4 ℃.

Detection of miRNA-155 by fluorescent probe MB-UCNP@SiO_2 + QDs

To investigate the practicality of the method, take 100ul of the fluorescent probe MB-UCNP@SiO_2 + QDs solution obtained from the above steps and reserve it. Prepare miRNA-155 solution with different concentrations (100 pM, 1 nM, 10 nM, 100 nM, 1 μM and 10 μM), take 20 ul of miRNA-155 solution with the above concentration of 100pM and add to 100ul of fluorescent probe solution and shake to mix, incubate for 40 min at room temperature and perform fluorescence spectroscopy measurement at the end of the reaction. The reaction was incubated for 40 min at room temperature, and the fluorescence spectra were measured at the end of the reaction, the remaining four concentrations of miRNA solutions were operated identically.

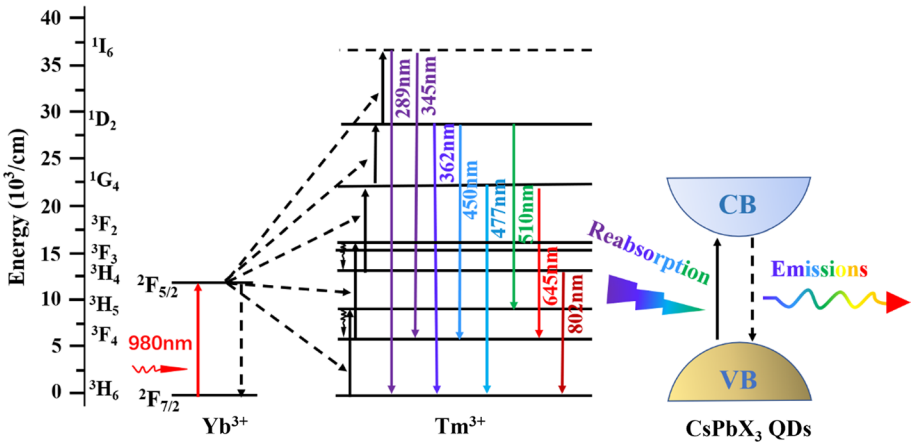

Fig. 2 Luminescence mechanism of the UCNP@SiO_2 + QDs composite material

Results and discussion

The luminescent mechanism of UCNP@SiO_2 + QDs composite material

UCNPs luminescence is a complex multi-photon energy transfer and conversion process. UCNPs under 980 nm excitation light excitation, 345 and 362 nm UV light originates from $^1I_6$ to $^3F_4$ energy level jump and $^1D_2$ to $^3H_6$ energy level jump, respectively. In the visible band, the purple band at 450 nm originates from the $^1D_2$ to $^3F_4$ energy transition, the blue band at 477 nm originates from the $^1G_4$ to $^3H_6$ energy transition, and the red band at 645 nm originates from the $^1G_4$ to $^3F_4$ energy transition. In the near-infrared band, the near-infrared light at 802 nm originates from the energy level jump from $^3H_4$ to $^3H_6$, and the doping ratio of UCNPs is $NaYF_4$: 20% Yb^{3+},0.5% Tm^{3+}@$NaYF_4$:10% Yb^{3+}, the luminescence mechanism of the UCNP@SiO_2 + QDs composite material is shown in Fig. 2.

The UCNP@SiO_2 + QDs composite material under the excitation of near-infrared 980 nm excitation light, the UCNPs as the donor and the QDs as the acceptor, the multicolor luminescence of the UCNPs is re-excited by the FRET to the QDs. The individual quantum dots may be adjusted by the doping ratio of different halogen elements (X = Cl, Br, I), which can achieve continuous modulation in the entire visible wavelength band, and QDs have an extremely narrow half-peak width of 12–37 nm, it proves that QDs have good monochromatic properties, which can achieve high fluorescence purity, The QDs doped with different ratios of halogen elements in the UCNP@SiO_2 + QDs composite can be precisely tuned in the full wavelength range of 400–700 nm to achieve tunable multicolor luminescence, and the reasonable design of the composite structure can be widely used in various fields.

Synthesis of UCNP@SiO_2

A typical high-temperature co-precipitation method was used to prepare UCNPs luminescent nanomaterials (Liu et al. 2018; (Wang et al. 2021a, b), the fluorescence spectra of UCNPs and UCNP@SiO_2 are shown in Fig. 3A. There were intense emission peaks in the UV and visible as well as near-infrared wavelength range, with an overall visible expression of blue radiation. The fluorescence peak position of UCNP@SiO_2 exhibited

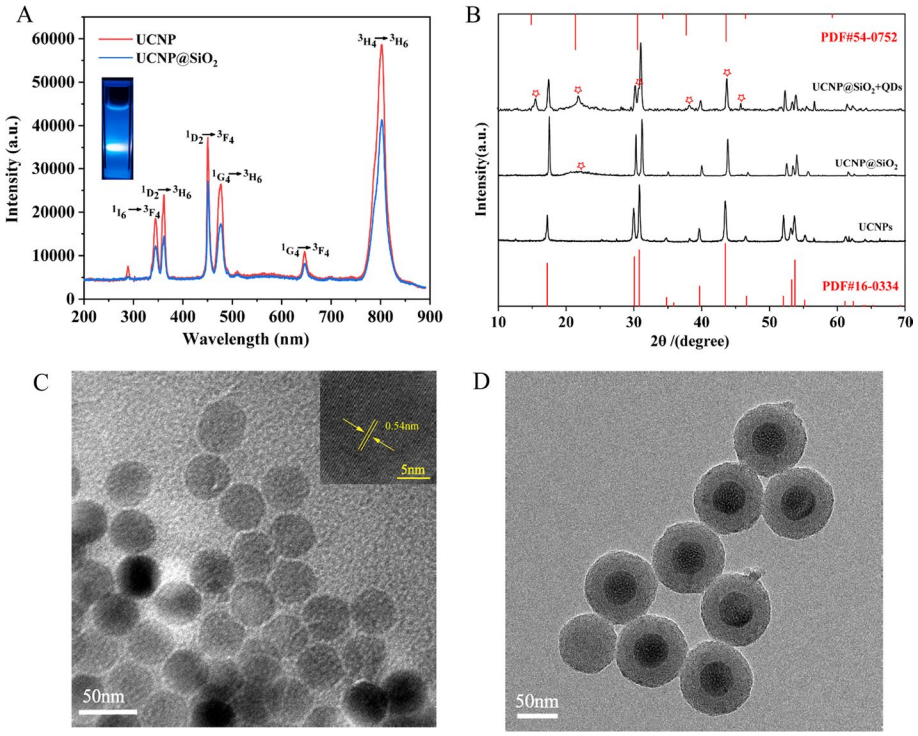

Fig. 3 Preparation and characterization of UCNP@SiO_2 nanomaterials. **A** Fluorescence spectrogram of UCNPs and UCNP@SiO_2, the excitation light wavelength is 980 nm. **B** XRD patterns of UCNPs@SiO_2 and UCNP@SiO_2 + QDs materials. **C** TEM image of UCNP. **D** TEM image of UCNP@SiO_2

no shift, only the fluorescence intensity decreased to 77% of the UCNP structure. The XRD pattern of UCNP@SiO_2 is shown in Fig. 3B, after coating with SiO_2, which was compared with the standard card of $NaYF_4$ (JCPDS NO 16–0334), the main diffraction peaks of the UCNPs material have not changed dramatically, and the obtained UCNPs@SiO_2 were compared with the standard card for amorphous SiO_2 (JCPDS 29–0085), with only a broad derivative peak within a 20–22° diffraction angle. And the growth of QDs in the mesoporous of SiO_2 to obtain the composite UCNP@SiO_2 + QDs, when compared with the standard card of $CsPbBr_3$ (JCPDS NO 54–0752), the structure of UCNP@SiO_2 + QDs has been added to the counterpart diffraction position with QDs, which has been marked with asterisks in the diagram, and the overall diffraction peak intensities of UCNP@SiO_2 + QDs are both relatively weakened, but there are no other more significant heterodyne peaks.

The TEM of UCNPs is shown in Fig. 3C. The whole structure of UCNPs nanomaterials was shell structure and could have better dispersion, the high-resolution TEM image of individual nanoparticles clearly showed lattice stripes with a spacing of 0.54 nm, and the UCNPs structure size was 38.2 nm. To ensure the effective distance between UCNPs and quantum dots, it was necessary to control the thickness of silica and mesopore size, the UCNPs surface was accompanied by a large amount of hydrophobic oleic acid, and a typical Stober method was used to prepare mesoporous silica (Kim et al. 2008; Yang et al. 2009), with UCNPs as the core and the mesoporous silica wrapped on the conversion structure using a structured guide (CTAB). The mesoporous silica had a high specific

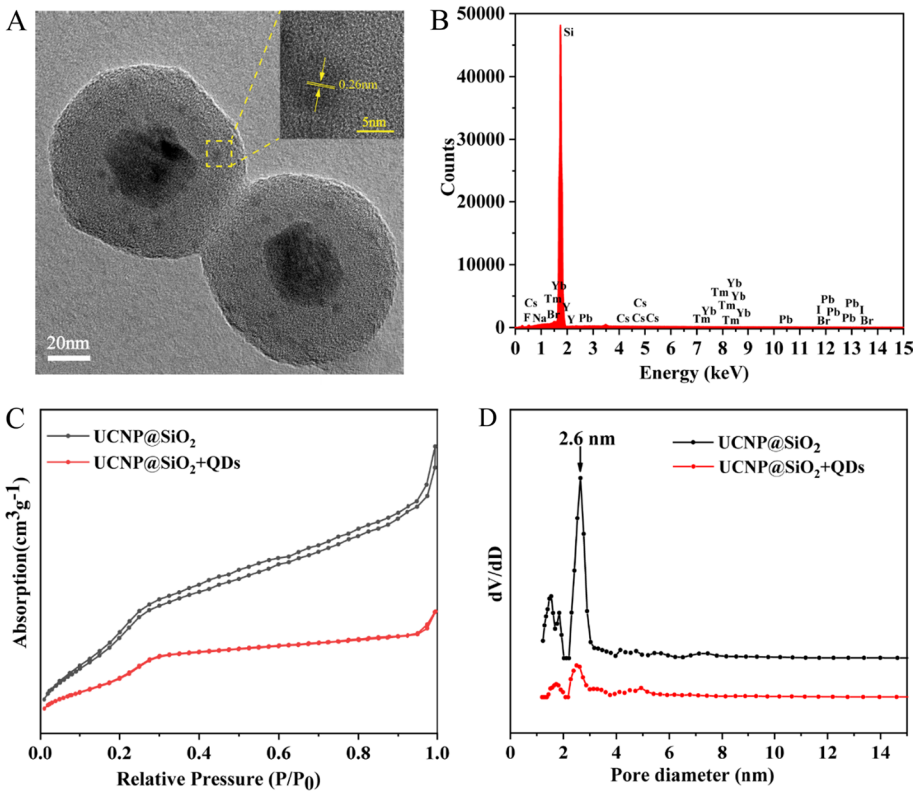

Fig. 4 Preparation and characterization of UCNP@SiO_2 + QDs composite materials. **A** TEM image of UCNP@SiO_2 + QDs. **B** EDS energy spectra of UCNP@SiO_2 + QDs. **C** N_2 isothermal adsorption and desorption curves of UCNP@SiO_2 and UCNP@SiO_2 + QDs. **D** Pore size distributions of UCNP@SiO_2 and UCNP@SiO_2 + QDs

surface area, strong adsorption and excellent stability properties. The TEM image of UCNP@SiO_2 is shown in Fig. 3D. Which showed that the number of small white holes and stripes, the particles were relatively transparent, and the overall size of UCNP@SiO_2 was 91.4 nm, at which point the overall luminescence intensity was reduced due to the thickness of the encapsulated silica, yet the overall luminescence performance remained good, which was accomplished with the measurement of UCNP@SiO_2 for QDs growth.

Synthesis and characterization of UCNP@SiO_2 + QDs

To ensure the effective combination of both UCNPs and QDs to yield the composite material UCNP@SiO_2 + QDs, mesoporous SiO_2 was used as the carrier, on the one hand, the mesopores made the energy transfer process achievable, and more importantly, enhanced the stability of QDs to water and oxygen environment, the SiO_2 mesopores were utilized to wrap and passivate the quantum dots, which further improved the stability of QDs to sensitive conditions. SiO_2 also provided better biocompatibility and water solubility of the whole composite material for the stability of sensitive surroundings. The TEM image of UCNP@SiO_2 + QDs is shown in Fig. 4A. It was obvious that the QDs were successfully grown in the mesopores, and the whole particles were composite material UCNP@SiO_2 + QDs. The high-resolution TEM image of a single nanoparticle clearly showed a lattice stripe with a d-spacing of 0.26 nm in the (200) plane,

this corresponded to the peak of the QDs structures at about 30 in the diffraction angle, and it equated with the lattice stripe pitch of the QDs individually constructed by heat injection. Which indicated that the growth of QDs was accomplished in the mesopores of SiO_2 (Xie et al. 2021; Wang et al. 2016a, b, 2022a, b; Xu et al. 2020). The protection of mesoporous Si secured the luminescence efficiency and stability of UCNP@SiO_2 + QDs in aqueous badlands. The EDS energy spectrum of UCNP@SiO_2 + QDs as shown in Fig. 4B, which showed the new elements of Cs, Pb, Br, and I in the distribution of UCNP@SiO_2 elements, and it indicated the existence of QDs on the surface of UCNP@SiO_2 appear.

To indicate whether QDs intervene in the mesopores of SiO_2, the specific surface area BET (Brunauer–Emmet–Teller) was used to comparatively analyze the changes in surface adsorption capacity and pore number before and after the addition of QDs in UCNP@SiO_2. N_2 isothermal adsorption and desorption curves are shown in Fig. 4C, when P/P_0 was larger than 0.28, the adsorption amount started to increase slowly, and the adsorption rate had kept steady. This indicates that the pore channel homogeneity was well and the pore size was small. The BET specific surface area and the pore volume of UCNP@SiO_2 were measured to be 935.264 $m^2\ g^{-1}$ and 1.116 $cm^3 g^{-1}$. After the growth of QDs in the mesopores of SiO_2, the BET specific surface area and the pore volume of UCNP@SiO_2 + QDs were measured to be 764.707 $m^2\ g^{-1}$ and 0.925 $cm^3\ g^{-1}$. Due to the entry of QDs into the mesopores, the specific surface area and pore volume were significantly lowered. The pore size distribution of UCNP@SiO_2 as shown in Fig. 4D, the number of pores on its surface was measured to be decreased, and the number of pores at the 2.6 nm position was significantly lowered. these variations could offer a powerful basis for the incorporation of QDs into the small size mesopores of UCNP@SiO_2.

Fluorescence properties of UCNP@SiO_2 + QDs

The fluorescence spectra of different halogen element ratios, as shown in Fig. 5A. The size of the QDs growing in the mesopores was less than 5 nm, which was slightly lower than the corresponding Bohr exciton diameter of 12 nm, due to the band gap and quantum confinement effect of QDs proper (Swarnkar et al. 2015; Protesescu et al. 2015), which makes the QDs emission peak appear to have a blue shift phenomenon, and the position of blue shift occurs at about 10 nm, and this phenomenon exists for all the other composite materials. Therefore, to obtain the ideal emission light, as far as possible, we choose the halogen element dosage ratio where the wavelength of the QDs original emission light is more than the desired emission light position of UCNP@SiO_2 + QDs, this will provide an accurate judgment for subsequent detection applications. The fluorescence chromatogram corresponding to the whole emission peak, as shown in Fig. 5B, and the chromatic colors corresponding to the various halogen element doping ratios have been marked in the diagrams. With reference to the marked positions for halogen element doping, which could yield any of the fluorescent colors in the visible wavelength band, achieving continuous tuning from the UV light to the red light, as compared to the emission lights of the UCNPs separately, the composites UCNP@SiO_2 + QDs have an emission light colors variety that far exceeds the full number of emission light colors of the UCNPs alone. Under the excitation of near-infrared light, the halogen element doping ratio and size effect of QDs can be used to control the luminescence

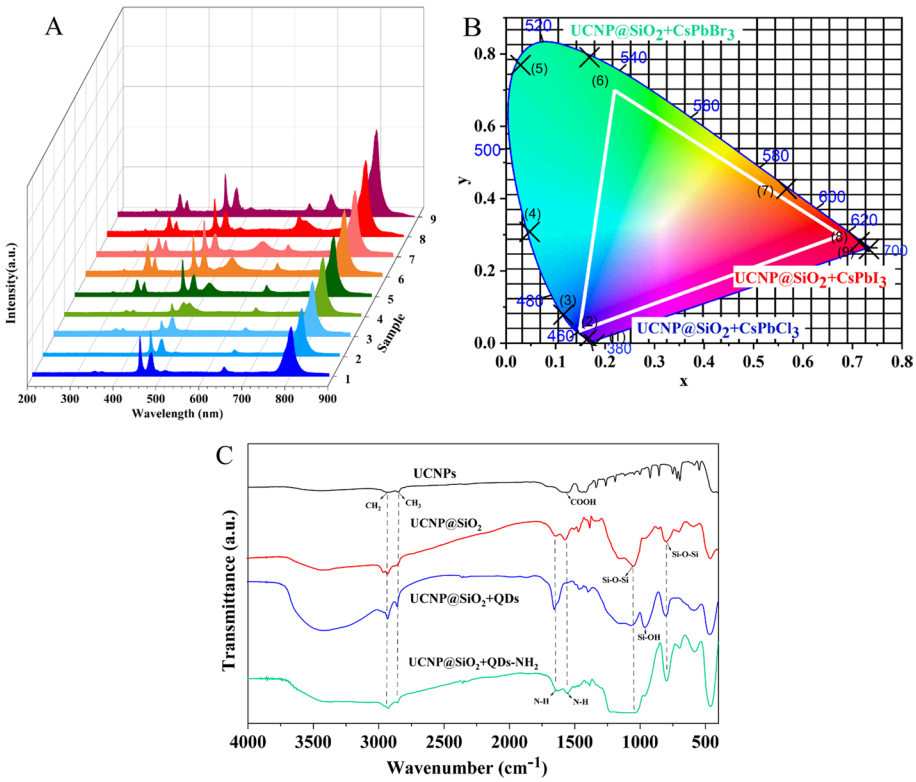

Fig. 5 Fluorescence properties of UCNP@SiO_2 + QDs composite materials. **A** Fluorescence spectrogram of UCNP@SiO_2 + QDs with different QDs (X = Cl, Br, I) doping ratios. (Sample: (1) UCNP@SiO_2 + QDs (Cl Br = 0.9: 0.1); (2) UCNP@SiO_2 + QDs (Cl Br = 0.7: 0.3); (3) UCNP@SiO_2 + QDs(Cl Br = 0.5: 0.5); (4) UCNP@SiO_2 + QDs(Cl Br = 0.3: 0.7); (5) UCNP@SiO_2 + QDs ($CsPbBr_3$); (6) UCNP@SiO_2 + QDs (Br:I = 0.7: 0.3); (7) UCNP@SiO_2 + QDs (Br:I = 0.5: 0.5); (8) UCNP@SiO_2 + QDs (Br:I = 0.3: 0.7); (9) UCNP@SiO_2 + QDs (Br:I = 0.1: 0.9), the excitation light wavelength is 980 nm). **B** CIE plots of UCNP@SiO_2 + QDs for Sample 1 to Sample 9. **C** FTIR spectra of UCNPs, UCNP@SiO_2 + QDs, UCNP@SiO_2 + QDs and UCNP@SiO_2 + QDs-NH_2

position of UCNP@SiO_2 + QDs composites continuously in the full wavelength range of 400–700 nm, which can be accurately modulated to the best luminescence peak position for detecting the target, to enhance the practical application efficiency of UCNP@SiO_2 + QDs composite material.

To illustrate the process of the change of the composite surface structure more clearly, the FTIR spectra of UCNP@SiO_2 + QDs are shown in Fig. 5C. In the process of SiO_2 wrapping and modifications of amino groups, the absorption peaks varied in intensity for each functional group or chemical bond stretching and bending vibration on the surface of the materials. The dashed lines in the diagram provided a convenient way to compare and evaluate the absorption properties of the functional groups at similar wave numbers. Exposed UCNPs with large amounts of oleic acid attached to the surfaces. the absorption peaks at 2935 cm^{-1} and 2852 cm^{-1} are due to the stretching vibrations of the surface oleic acid ligands CH_2 and CH_3, respectively, and the asymmetrical stretching vibrations of the carboxylate COOH molecule of the oleic acid at 1562 cm^{-1}. The peaks at 1047 cm^{-1} and 795 cm^{-1} are from the stretching and bending vibrations of Si–O–Si stretching and bending vibrations, suggesting that the structure of SiO_2 has been encapsulated on the surface of the upconverted UCNPs. Using the trace hydrolysis of APTES for amide functionalization on

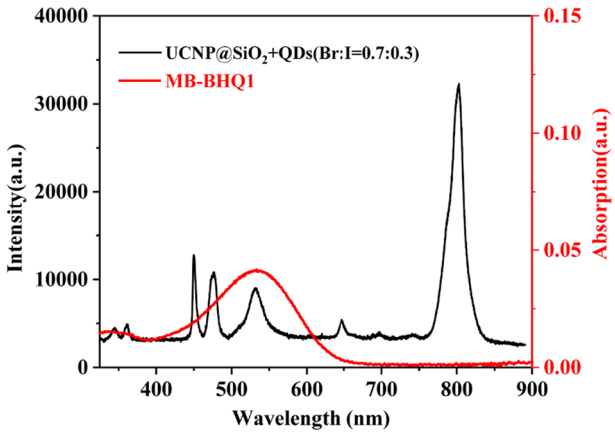

Fig. 6 Fluorescence spectra of UCNP@SiO_2 + QDs (Br: I = 0.7:0.3) and absorption spectra of MB-BHQ1

the surface of UCNP@SiO_2 + QDs, the weak absorption band at 956 cm^{-1} was Si–OH stretching, indicating that a hydrolytic condensation process of APTES had occurred on the surface of the material, and the absorption peaks at 1543 cm^{-1} and 1654 cm^{-1} were from bending vibrations of the N–H bond in the NH_2 groups. This further demonstrated that amination was achieved on its surface and obtained the aminated UCNP@SiO_2 + QDs composite material.

Characterization of UCNP@SiO_2 + QDs (br:I = 0.7:0.3)

In the structure of the fluorescent probe we designed, the quencher attached to the molecular beacon MB is the BHQ1 quenching group, which has a wide range of absorption peaks at 532 nm, and we have to match the absorption spectrum of BHQ1 by modulating the specific halogen element doping ratio of the composite. Under the 980 nm light source excitation, by specific evaluation of the position of the emitted light of UCNP@SiO_2 + QDs, at a halogen element doping ratio of Br: I = 0.7: 0.3, the position of the new emitted light produced by UCNP@SiO_2 + QDs (Br: I = 0.7: 0.3) is at 531 nm. the absorption spectrum of MB-BHQ1 and UCNP@SiO_2 + QDs (Br: I = 0.7: 0.3) fluorescence spectra have achieved the maximum overlap, as shown in Fig. 6. Taking advantage of the hairpin-type structure of MB proper, the BHQ1 quenching group can achieve the best level of quenching for the 531 nm luminescence. As a result, we finally selected a halogen doping ratio as Br: I = 0.7: 0.3. The detection of UCNP@SiO_2 + QDs (Br: I = 0.7: 0.3) and the BHQ1 quenching group was designed by connecting the two sides of MB, according to the fluorescence intensity at the 531 nm position to complete the detection of miRNA-155.

According to the previously descriptive interpretation, here the luminescence process of UCNP@SiO_2 + QDs is investigated further in conjunction with the absorption spectra of QDs (Br: I = 0.7:0.3). The fluorescence spectra of UCNP@SiO_2 and the absorption spectra of QDs (Br: I = 0.7:0.3) are shown in Fig. 7A. The emission peaks of UCNP@SiO_2 at 345 nm, 362 nm, 450 nm, and 477 nm position of the emission peaks overlap with the strong absorption range of QDs, which makes QDs multi-photon absorption of the luminescence of UCNP@SiO_2. Under the excitation of 980 nm near-infrared light, the FRET occurs between both UCNPs and QDs, and the multi-emission light of UCNPs

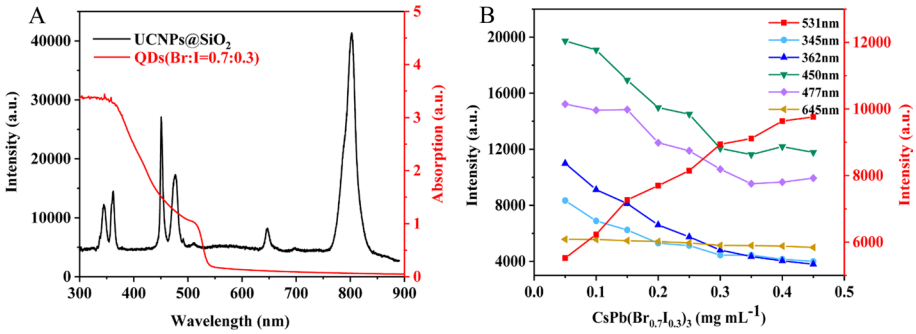

Fig. 7 Characterization of UCNP@SiO_2 + QDs (Br: I = 0.7: 0.3) materials. **A** Fluorescence spectrum of UCNP@SiO_2 and absorption spectrum of separate of QDs (Br: I = 0.7: 0.3). **B** Schematic diagram of the relationship between the intensity of the corresponding luminescence peaks of UCNP@SiO_2 + QDs with different concentrations of QDs (Br: I = 0.7: 0.3), the excitation light wavelength is 980 nm

excited the luminescence of QDs again synergistically, the position of the luminous peak of the desired target could be obtained. To achieve the best conversion efficiency of both UCNP@SiO_2 and QDs (Br: I = 0.7:0.3), UCNP@SiO_2 was combined with various concentrations of QDs (Br: I = 0.7:0.3) to obtain the various graphs of UCNP@SiO_2 + QDs at each peak value (Melle et al. 2018).

As the concentration of QDs in UCNP@SiO_2 + QDs increases, the light intensity at the 531 nm position is gradually increased, mainly at the sacrifice of UV and blue light, and the UV intensity at 345 and 362 nm decreases much faster than the blue emission intensity at 450 and 477 nm, while the red emission at 645 nm is nearly changeless. This may be attributed to the much larger absorbance of QDs in the UV than in the blue and almost no absorption in the red, which is shown in Fig. 7B. To ensure the structural stability of UCNP@SiO_2 + QDs and to maintain the strong luminescence intensity of UCNP@SiO_2 + QDs at 531 nm, QDs (Br: I = 0.7: 0.3) at a concentration of 0.3 mg/ml is chosen as the best level, and the FRET efficiency of both of them is obtained up to 70.6%. It can be shown that there is a high energy conversion efficiency between UCNPs and QDs.

Synthesis and optimization of MB-UCNP@SiO_2 + QDs fluorescent probes

MB was directly attached to the surface of UCNP@SiO_2 + QDs via a chemical bond, which allowed the BHQ1 quenching group to be close to the surface of the material, the 5' side of the MB chain was modified with COOH and the BHQ1 quenching group was modified at the 3' side, and the maximum distance between the surface of UCNP@SiO_2 + QDs and the BHQ1 quenching group was 0.68 nm. (According to the length of one base pair), this distance was much smaller than the effective action distance of FRET at 10 nm, so it made the fluorescence quenching occur, the fluorescence quenching effect of MB-UCNP@SiO_2 + QDs fluorescent probe at the position of 531 nm was obtained, and the energy transfer efficiency was obtained to be 66.3%, which reduced the fluorescence background signal of the probe itself. The fluorescence characteristics of MB-UCNP@SiO_2 + QDs fluorescence probe sensing are shown in Fig. 8A, and the normalized fluorescence intensity is plotted in Fig. 8B. When the fluorescent probe was linked to the neutral miRNA-155, the structural loop of the MB-155 was

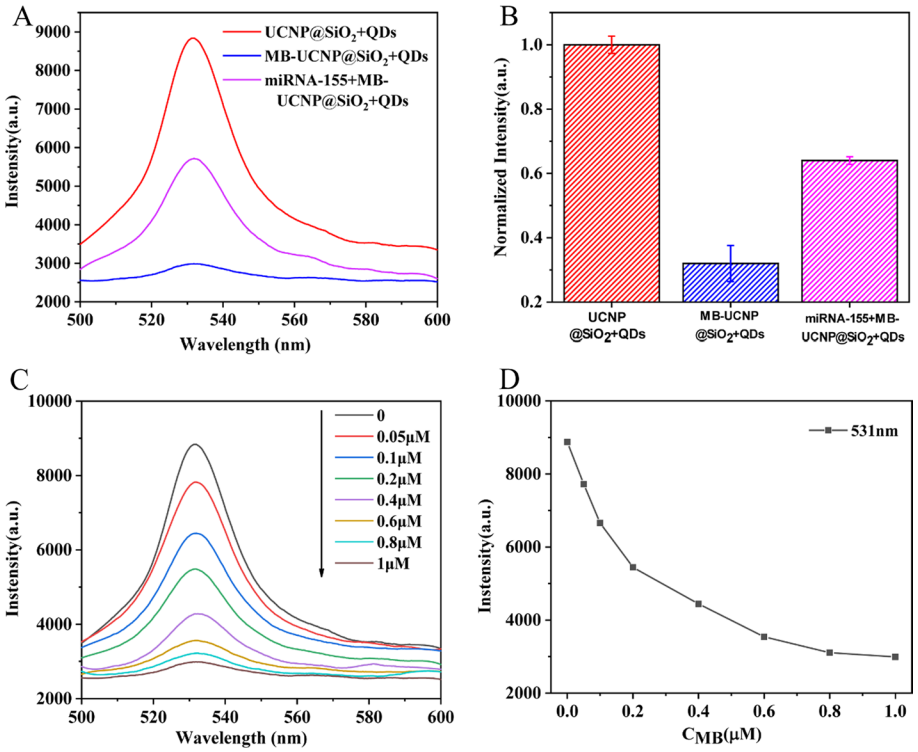

Fig. 8 Fluorescence characteristics of the fluorescent probe MB-UCNP@SiO_2 + QDs. **A** The sensing process of MB-UCNP@SiO_2 + QDs fluorescent probes. **B** The normalized fluorescence intensity in **A**. **C** Fluorescence spectra of MB-UCNP@SiO_2 + QDs at 531 nm with different MB concentrations. **D** Profiles of fluorescence peak intensity variation from the corresponding spectra in **C**

opened, causing the BHQ1 quenching group to move away from the surface of UCNP@SiO_2 + QDs. The maximum distance between the surface of UCNP@SiO_2 + QDs and the BHQ1 quenching group was calculated to be 11.9 nm. (According to the number of bases of MB length), which was greater than the effective action distance of FRET at 10 nm. This made the partial fluorescence of UCNP@SiO_2 + QDs at the 531 nm position recovered, and the efficiency of energy transfer at this time was obtained to be 35.6%. It did not complete recovery, probably because there was still a partial fluorescence burst mechanism of energy radiative transfer, and the UCNP@SiO_2 + QDs released the excitation energy in the form of radiation and returned to the ground state itself.

UCNP@SiO_2 + QDs were shielded with mesoporous silica. For further enhancing the stability of UCNP@SiO_2 + QDs to sensitive conditions, we used a slightly weaker polar 75% ethanol solution as the reaction solvent. To optimize the configuration of fluorescent probes, MB-UCNP@SiO_2 + QDs fluorescent probes were generated based on the same volume of 80u l of aminated UCNP@SiO_2 + QDs with 20ul of different concentrations (0.05, 0.1, 0.2, 0.4, 0.6, 0.8, and 1 μM) of MB solution, and the fluorescence detection of the probes was performed. The fluorescent spectra as shown in Fig. 8C. Figure 8D depicted the change curve of fluorescence intensity at 531 nm as MB concentration increased, and when the concentration of MB increased to 1 μM, the light intensity was basically stable and remained unchanged, indicating that the fluorescence had been

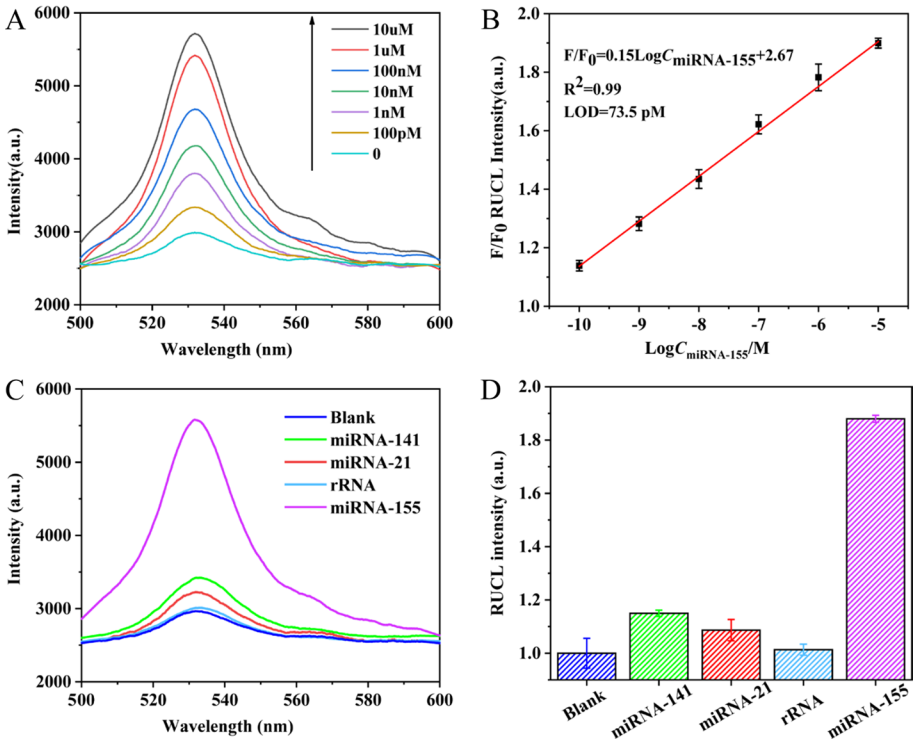

Fig. 9 Detection of miRNA-155 with fluorescent probes of MB-UCNP@SiO_2 + QDs. **A** Plots of fluorescence spectra for the detection of different miRNA-155 concentrations. **B** Plot of the relationship between the fluorescence intensity ratio and the logarithm of miRNA-155 concentration. **C** Plots of fluorescence spectra for the detection of miRNAs with different base sequences. **D** Histogram of fluorescence peak intensities for the corresponding spectra shown in **C**. The error bars represent the standard deviation from the three measurements

quenched to the maximum extent. so that the optimal concentration of MB was 1 μM, and this concentration of MB-155 fluorescence was used.

Detection of miRNA-155 with fluorescent probe MB-UCNP@SiO_2 + QDs

Equal volumes of 20 μL of miRNA-155 solutions with different concentrations (100 pM, 1 nM, 10 nM, 100 nM, 1 μM, and 10 μM) were prepared and connected to the fluorescent probe MB-UCNP@SiO_2 + QDs, which is shown in Fig. 9A. The relationship between the logarithm of miRNA-155 concentration (logCmiRNA-155) and the fluorescence intensity ratio (F/F_0) was plotted in Fig. 9B, with F_0 represented the fluorescence intensity of MB-UCNP@SiO_2 + QDs and F represented the fluorescence intensity of miRNA-155 + MB-UCNP@SiO_2 + QDs, it could be observed that from 100 pM to 10 μM miRNA-155 concentration followed the linear fitting curve $F/F_0 = 0.15 \times \log C_{miRNA-155} + 2.67$ ($R^2 = 0.99$), according to the definition of the limit of detection (LOD) 3σ/s the LOD of miRNA-155 was calculated to be 73.5 pM, here σ is the standard deviation of F/F_0 and s is the linear equation of the slope.

To analyze the effect of fluorescent probes on the detection of specific recognition of different miRNAs, we selected other markers in the process of malignant proliferation expression of tumor cells as comparisons, which were used for further

Table 1 Nucleotide sequences of miRNAs and MB in fluorescent probes

name	Sequences (5′–3′)
miRNA-155	UUAAUGCUAAUCGUGAUAGGGGU
MB-155	COOH-ATAGCGACCCCTATCACG ATTAGCATTAACGCTAT-BHQ1
miRNA — 141	UAACACUGUCUGGUAAAGAUGG
miRNA — 21	UAGCUUAUCAGACUGAUGUUGA
rRNA	AUAUACGAUUAGCACUAUCUCA

Table 2 Comparison of the performance of the established fluorescent probes and the reported similar fluorescent probes

Energy donor	Energy acceptor	Target	Linear range (nM)	Detection limit (nM)	Refs
UCNPs	Cy3	miRNA-21	0.2–1.4	0.095	(Zhu et al. 2018)
UCNPs	BHQ3	miRNA-21	50–500	2	(Wang et al. 2018)
UCNPs	TAMRA	DNA	40–200	2.8	(Zhu et al. 2015)
UCNPs	MoS_2	miRNA-155	50–500	0.25	(Wu et al. 2021)
UCNPs, QDs	BHQ1	miRNA-155	0.1–10000	0.0735	This work

experiments using miRNA-155, miRNA-141, miRNA-21 and random rRNA sequence samples. MB-155 and the base sequences of other miRNAs are shown in Table 1.

Different base sequences of the target with the same concentration of 1 μM were formulated and the fluorescence spectra were obtained as shown in Fig. 9C, and the fluorescence peaks of the five fluorescence spectra were plotted as bar graphs as shown in Fig. 9D. It could be seen that the degree of fluorescence recovery was different, with the maximum fluorescence recovery signal for normal miRNA-155 and nearly absent for random rRNA. Which indicated that the prepared fluorescent probes have good specific recognition in the detection. Even a few single or individual mismatched bases on miRNA-155 can be detected, and it could specifically distinguish miRNA-155 from miRNA with mismatched sequences, which could provide a strong basis for the early diagnosis of diseases such as cancer and tumors. The performance of the constructed nanoprobes was compared with similarly reported UCNPs nanoprobes (Table 2). The detection limits of the established fluorescent probes were equal to or lower than the detection limits of other fluorescent probes.

Conclusions

In summary, a novel fluorescent probe based on the combination of UCNPs nanomaterials and QDs was developed to achieve the specific recognition and low concentration detection of miRNA-155. Under the excitation of 980 nm near-infrared light, through tuning the doping ratio of QDs halogen elements in the composite material UCNP@SiO_2 + QDs, which achieved the tunable and precise luminescence of UCNP@SiO_2 + QDs in the full wavelength range of visible light. The novel fluorescent probe MB-UCNP@SiO_2 + QDs was prepared through the use of MB with UCNP@SiO_2 + QDs and BHQ1 quenching groups attached to the two sides of MB, which accomplished the

detection of miRNA-155 at low concentration and obtained a detection limit of 73.5 pM. Simultaneously, it could enable the specific differentiated detection of miRNAs with different base sequences. The reasonable design of the new composite nanomaterials can realize multi-color luminescence with tunable and high stability, and it can have a huge potential and important significance in many fields, such as multi-color fluorescence imaging, multi-mode luminescence anti-counterfeiting, and biofluorescent probe detection.

Abbreviations

UCNPs	Rareearth upconversion
QDs	Perovskite quantum dots
MB	Molecularbeacon
BHQ1	Blackhole quencher-1
FRET	Fluorescence resonance energy transfer
CTAB	CetyltrimethylammoniumBromide
APTES	3-Amino propyl triethoxy silane
EDC	1-Ethyl-(3-dimethylaminopropyl) diimine carbonate hydrochloride
NHS	N-hydroxy succinimide
XRD	X-ray diffraction
TEM	Transmission electron microscope
BET	Brunauer–Emmett–Teller
CIE	Commissioninternationale de l'eclairage
EDS	Energy dispersive spectroscopy
FTIR	Fourier transform infrared

Acknowledgements
Not applicable.

Author contributions
YH, HTR and JJW contributed conceptualization, methodology and investigation. CCY, HT and LZ contributed for methodology, formal analysis, data curation and editing YW and CQH did formal analysis, data curation and editing. YL and WC are in charge of conceptualization, visualization, supervision, and funding as well as writing and editing, validation for submission. All authors have read and approved the final the manuscript.

Funding
This work was supported by the National Natural Science Foundation of China (NO. 61971207), the Natural Science Foundation of the Jiangsu Higher Education Institutes of China (NO. 19KJA510003 and NO. 20KJA430003), and the Postgraduate Research & Practice Innovation Program of Jiangsu Normal University (NO. 2021XKT1210).

Availability of data and materials
Not applicable.

Declarations

Ethics approval and consent to participate
Not applicable.

Consent for publication
Not applicable.

Competing interests
The authors declare that they have no competing interests.

Received: 26 November 2022 Accepted: 28 April 2023
Published online: 12 May 2023

References

Chen W (2020) Nanoparticle fluorescence based technology for biological applications. J Nanosci Nanotechnol 8(3):1019–1051
Chen P, Liu Y, Zhang Z, Sun Y, Hou J, Zhao G et al (2019) In situ growth of ultrasmall cesium lead bromine quantum dots in a mesoporous silica matrix and their application in flexible light-emitting diodes. Nanoscale 11(35):16499–16507
Chien H, Tsai M, Yang C, Lee R, Wang T (2020) Interaction of $LiYF_4$:Yb^{3+}/Er^{3+}/Ho^{3+}/Tm^{3+}@$LiYF_4$: Yb $^{(3+)}$ upconversion nanoparticles, molecularly imprinted polymers, and templates. Rsc Adv 10(59):35600–35610

Cu F, Qiu Q, Peng G, Li X, Liu X, Chen X (2019) Core-shell CdSeTe/ZnS quantum dots for the detection of microRNA-155 based on the fluorescence resonance energy transfer technique via the formation of a network structure. Anal Methods 11(32):4137–4145

Ding Z, He Y, Rao H, Zhang L, Nguyen W, Wang J et al (2022) Novel fluorescent probe based on rare-earth doped upconversion nanomaterials and its applications in early cancer detection. Nanomaterials 12(11):1787

Dirin D, Protesescu L, Trummer D, Kochetygov I, Yakunin S, Krumeich F et al (2016) Harnessing defect-tolerance at the nanoscale: highly luminescent lead Halide perovskite nanocrystals in Mesoporous silica matrixes. Nano Let 16(9):5866–5874

Fan Y, Liu L, Zhang F (2019) Exploiting lanthanide-doped upconversion nanoparticles with core/shell structures. Nano Today 25:68–84

Gao CJ, Zheng PR, Liu QX, Han S, Li DL, Luo SY et al (2021) Recent advances of upconversion nanomaterials in the biological field. Nanomaterials 11(10):2474

Huang S, Tan L, Zhang L, Wu J, Zhang L, Tang Y et al (2020) Molecularly imprinted mesoporous silica embedded with perovskite $CsPbBr_3$ quantum dots for the fluorescence sensing of 2,2-dichlorovinyl dimethyl phosphate. Sens Actuators B-Chem 325:15

Hwang D, Song I, Lee D, Kim S (2010) Smart magnetic fluorescent nanoparticle Imaging probes to monitor microRNAs. Small 6(1):81–88

Ke J, Lun M, Jigang, Wang et al (2013) Graphene oxide and reduced graphene oxide: synthesis, photoluminescence, and biotechnological applications. Rev in Nanosci Nanotechnol 2(3):171–183

Kim J, Kim HS, Lee N, Kim T, Kim H, Yu T et al (2008) Multifunctional uniform nanoparticles composed of a magnetite nanocrystal core and a mesoporous silica shell for magnetic resonance and fluorescence imaging and for drug delivery. Angew Chem-Int Edit 47(44):8438–8441

Kowada T, Maeda H, Kikuchi K (2015) BODIPY-based probes for the fluorescence imaging of biomolecules in living cells. Chem Soc Rev 44(14):4953–4972

Labib M, Ghobadloo S, Khan N, Kolpashchikov D, Berezovski M (2013) Four-Way Junction formation promoting ultrasensitive electrochemical detection of microRNA. Anal Chem 85(20):9422–9427

Li C, Quan Z, Yang J, Yang P, Lin J (2007) Highly uniform and monodisperse beta-$NaYF_4$: $In^{(3+)}$ (In = Eu/Tb, Yb/Er, and Yb/Tm) hexagonal microprism crystals: hydrothermal synthesis and luminescent properties. Inorg Chem 46(16):6329–6337

Li X, Wu Y, Zhang S, Cai B, Gu Y, Song J et al (2016) $CsPbX_3$ quantum dots for lighting and displays: room-temperature synthesis, photoluminescence superiorities, underlying origins and white light-emitting diodes. Adv Funct Mater 26(15):2435–2445

Li XM, Zhang HC, Tang YR, Wu P, Xu SX, Zhang XF (2017) A both-end blocked peroxidase-mimicking DNAzyme for low-background chemiluminescent sensing of miRNA. Acs Sens 2(6):810–816

Li W, Wang T, Zheng C, Guo L, Chen W (2020) Composition-dependent optical limiting behavior of all-inorganic halide perovskite quantum dots. Opt Mater 110:110521

Li SQ, Zhang YT, Zu YX, Chen YT, Luo F, Huang D et al (2022) Photothermal sensor based on water-soluble CsPbBr3@sulfobutylether-beta-cyclodextrins nanocomposite using a thermometer as readout. Sens Actuators B-Chem 355:131301

Lim L, Lau N, Garrett-Engele P, Grimson A, Schelter J, Castle J et al (2005) Microarray analysis shows that some microRNAs downregulate large numbers of target mRNAs. Nat 433(7027):769–773

Liu H, Li K, Hu X, Zhu L, Rong Q, Liu Y et al (2017a) In situ localization of enzyme activity in live cells by a molecular probe releasing a precipitating fluorochrome. Angew Chem-Int Ed 56(39):11788–11792

Liu Q, Ma C, Liu X, Wei Y, Mao C, Zhu J (2017b) A novel electrochemiluminescence biosensor for the detection of microRNAs based on a DNA functionalized nitrogen doped carbon quantum dots as signal enhancers. Biosens Bioelectron 92:273–279

Liu X, Zhang SQ, Cheng ZH, Wei X, Yang T, Yu YL et al (2018) Highly sensitive detection of MicroRNA-21 with ICPMS via hybridization accumulation of upconversion nanoparticles. Anal Chem 90(20):12116–12122

Lu L, Wu Z, Li X, Han F (2019) State-of-the-art: functional fluorescent probes for bioimaging and pharmacological research. Acta Pharmacol Sin 40(6):717–723

Lv Y, Huang Z, Lin Y, Fang Y, Chen Z, Pan L et al (2019) MiRNA expression patterns are associated with tumor mutational burden in lung adenocarcinoma. Oncoimmunology 8(10):1–8

Ma D, Huang C, Zheng J, Tang J, Li J, Yang J et al (2018) Quantitative detection of exosomal microRNA extracted from human blood based on surface-enhanced Raman scattering. Biosens Bioelectron 101:167–173

Ma Y, Wei Y, Jiang F, Liu Y, Hong M (2022) Photon upconversion of all-inorganic $CsPbX_3$ quantum dots based on fluorescence resonance energy transfer in hetero-structured perovskite/upconversion nanocomposites. J Lumin 242:118565

Malgras V, Tominaka S, Ryan J, Henzie J, Takei T, Ohara K et al (2016) Observation of quantum confinement in monodisperse methylammonium lead halide Perovskite nanocrystals embedded in Mesoporous silica. J Am Chem Soc 138(42):13874–13881

Mao L, Lu Z, He N, Zhang L, Deng Y, Duan D (2017) A new method for improving the accuracy of miRNA detection with $NaYF_4$:Yb,Er upconversion nanoparticles. Sci China-Chem 60(1):157–162

Martynenko I, Litvin A, Purcell-Milton F, Baranov A, Fedorov A, Gun'ko Y (2017) Application of semiconductor quantum dots in bioimaging and biosensing. J Mater Chem B 5(33):6701–6727

Melle S, Calderon O, Laurenti M, Mendez-Gonzalez D, Egatz-Gomez A, Lopez-Cabarcos E et al (2018) Forster resonance energy transfer distance dependence from upconverting nanoparticles to quantum dots. J Phys Chem C 122(32):18751–18758

Meng C, Yang D, Wu Y, Zhang X, Zeng H, Li X (2020) Synthesis of single $CsPbBr_3$@SiO_2 core-shell particles via surface activation. J Mater Chem C 8(48):17403–17409

Pandey NK, Xiong W, Wang LY, Chen W, Bui B, Yang J et al (2022) Aggregation-induced emission luminogens for highly effective microwave dynamic therapy. Bio Mater 7:112–125

Protesescu L, Yakunin S, Bodnarchuk MI, Krieg F, Caputo R, Hendon CH et al (2015) Nanocrystals of cesium lead halide perovskites (CsPbX3, X = cl, br, and I): novel optoelectronic materials showing bright emission with wide color gamut. Nano Lett 15(6):3692–3696

Shan J, Kong W, Wei R, Yao N, Ju Y (2010) An investigation of the thermal sensitivity and stability of the beta-NaYF4:Yb, Er upconversion nanophosphors. J Appl Phys 107(5):937

Stanisavljevic M, Krizkova S, Vaculovicova M, Kizek R, Adam V (2015) Quantum dots-fluorescence resonance energy transfer-based nanosensors and their application. Biosens Bioelectron 74:562–574

Swarnkar A, Chulliyil R, Ravi VK, Irfanullah M, Chowdhury A, Nag A (2015) Colloidal $CsPbBr_3$ Perovskite Nanocrystals: luminescence beyond traditional Quantum dots. Angew Chem-Int Edit 54(51):15424–15428

Tang XD, Yu HM, Bui B, Wang LY, Xing C, Wang SY et al (2021) Nitrogen-doped fluorescence carbon dots as multi-mechanism detection for iodide and curcumin in biological and food samples. Bio Mater 6(6):1541–1554

Wang H, Lin S, Tang A, Singh B, Tong H, Chen C et al (2016a) Mesoporous silica particles integrated with all-inorganic CsPbBr3 perovskite quantum-dot nanocomposites (MP-PQDs) with high stability and wide color gamut used for backlight display. Angew Chem-Int Edit 55(28):7924–7929

Wang Y, He J, Chen H, Chen J, Zhu R, Ma P et al (2016b) Ultrastable, highly luminescent organic-inorganic Perovskite-Polymer Composite Films. Adv Mater 28(48):10710

Wang G, Fu YK, Ren ZH, Huang J, Best S, Li X et al (2018) Upconversion nanocrystal "armoured' silica fibres with superior photoluminescence for miRNA detection. Chem Commun 54(49):6324–6327

Wang T, Wei X, Zong Y, Zhang S, Guan W (2020) An efficient and stable fluorescent sensor based on APTES-functionalized $CsPbBr_3$ perovskite quantum dots for ultrasensitive tetracycline detection in ethanol. J Mater Chem C 8(35):12196–12203

Wang JH, Chen HY, Chuang CC, Chen JC (2021a) Study of near-infrared light-induced excitation of upconversion nanoparticles as a vector for non-viral DNA delivery. RSC Adv 11(2):807–808

Wang W, Guo R, Xiong X, Liu H, Chen W, Hu S et al (2021b) Improved stability and efficiency of perovskite via a simple solid diffusion method. Mater Today Phys 18:100374

Wang C, Zhang C, Wang F, Chen J, Kong J, Li L et al (2022a) Flexible cesium lead halide CsPbX3@SiO2 (X = cl, br, I and their mixtures) perovskite nanocrystal films. J Alloys Compd 925:166551

Wang JJ, Liu Y, Ding Z, Zhang L, Han CQ, Yan CC et al (2022b) The exploration of quantum dot-molecular beacon based MoS2 fluorescence probing for myeloma-related Mirnas detection. Bio Mater 17:360–368

Wu X, Li Y, Yang MY, Mao CB (2021) Simultaneous ultrasensitive detection of two breast cancer microRNA biomarkers by using a dual nanoparticle/nanosheet fluorescence resonance energy transfer sensor. Mater Today Adv 12:100163

Xie L, Hong Z, Zan J, Wu Q, Yang Z, Chen X et al (2021) Broadband detection of X-ray, ultraviolet, and near-Infrared photons using solution-processed perovskite-lanthanide nanotransducers. Adv Mater 33(25):2101852

Xu Y, Lou S, Xia C, Xuan T, Li H (2020) Controllable synthesis of all inorganic lead halide perovskite nanocrystals and white light-emitting diodes based on $CsPbBr_3$ nanocrystals. J Lumin 222:117132

Xu Y, Yu HM, Chudal L, Pandey NK, Amador EH, Bui B et al (2021) Striking luminescence phenomena of carbon dots and their applications as a double ratiometric fluorescence probes for H2S detection. Mater Today Phys 17:100328

Yang P, Quan Z, Hou Z, Li C, Kang X, Cheng Z et al (2009) A magnetic, luminescent and mesoporous core-shell structured composite material as drug carrier. Biomaterials 30(27):4786–4795

Yun R, Luo L, He J, Wang J, Li X, Zhao W et al (2021) Tunable and white up-conversion emission from Tm^{3+}-Ho^{3+}-Yb^{3+}/-Nd^{3+} co-doped $GdVO_4$ phosphors under 808-nm excitation. J Mater Sci-Mater Electron 32(6):8149–8156

Zhang H, Wang X, Liao Q, Xu Z, Li H, Zheng L et al (2017) Embedding perovskite nanocrystals into a polymer matrix for tunable luminescence probes in cell imaging. Adv Fun Mater 27(7):1604382

Zhang J, Yang Y, Jiang X, Dong C, Song C, Han C et al (2019) Ultrasensitive SERS detection of nucleic acids via simultaneous amplification of target-triggered enzyme-free recycling and multiple-reporter. Biosens Bioelectron 141:111402

Zhang JJ, Song CY, Zhou HL, Jia J, Dai YN, Cui DX et al (2020) A dual signal amplification strategy for the highly sensitive fluorescence detection of nucleic acids. Analyst 145(4):1219–1226

Zheng W, Huang P, Gong Z, Tu D, Xu J, Zou Q et al (2018) Near-infrared-triggered photon upconversion tuning in all-inorganic cesium lead halide perovskite quantum dots. Nat Commun 9(1):3462

Zhou W, Tian YF, Yin BC, Ye BC (2017) Simultaneous surface-enhanced Raman Spectroscopy detection of multiplexed MicroRNA biomarkers. Anal Chem 89(11):6121–6129

Zhu H, Ding YJ, Wang AQ, Sun X, Wu XC, Zhu JJ (2015) A simple strategy based on upconversion nanoparticles for a fluorescent resonant energy transfer biosensor. J Mater Chem B 3(3):458–464

Zhu D, Miao ZY, Hu Y, Zhang XJ (2018) Single-step, homogeneous and sensitive detection for microRNAs with dual-recognition steps based on luminescence resonance energy transfer (LRET) using upconversion nanoparticles. Biosens Bioelectron 100:475–481

Publisher's Note